

Opacity limit for supermassive black hole seeds

Fernando Becerra^{1*}, Federico Marinacci², Kohei Inayoshi³, Volker Bromm⁴ and Lars E. Hernquist¹

¹ *Harvard-Smithsonian Center for Astrophysics, 60 Garden Street, Cambridge, MA 02138, USA*

² *Kavli Institute for Astrophysics and Space Research, Massachusetts Institute of Technology, Cambridge, MA 02139, USA*

³ *Department of Astronomy, Columbia University, 550 W. 120th Street, New York, NY 10027, USA*

⁴ *Department of Astronomy, The University of Texas at Austin, TX 78712, USA*

15 February 2017

ABSTRACT

We present a model for the evolution of supermassive black hole seeds from their formation at $M_\star \simeq 0.1 M_\odot$ until their growth to $M_\star \simeq 10^5 M_\odot$. To calculate the initial properties of the object in the optically thick regime we follow two approaches: one based on idealized thermodynamic considerations, and one on a more detailed one-zone model. Both methods derive a similar value of $n_F \simeq 2 \times 10^{17} \text{ cm}^{-3}$ for the density of the object when opacity becomes important, i.e. the opacity limit. The subsequent evolution of the growing protostar is determined by the accretion of gas onto the object and can be described by a mass-radius relation of the form $R_\star \propto M_\star^{1/4}$. For the case of a supermassive black hole seed, this implies that the radius of the star grows from $R_\star \simeq 0.65 \text{ au}$ to $R_\star \simeq 65 \text{ au}$ during its evolution. Finally, we use this model to construct a sub-grid recipe for accreting sink particles in numerical simulations. A prime ingredient thereof is a physically motivated prescription for the accretion radius and the effective temperature of the growing protostar, embedded inside it. From the latter, we can conclude that photo-ionization feedback can be neglected until very late in the assembly process of the supermassive object.

Key words: hydrodynamics – stars: formation – galaxies: formation – galaxies: high-redshift – cosmology: theory – early Universe.

1 INTRODUCTION

Recent observations at redshifts $z \gtrsim 6$ suggest that quasars were already powered by supermassive black holes (SMBHs) with masses $\gtrsim 10^9 M_\odot$ when the Universe was less than one billion years old (Fan et al. 2003, 2006; Mortlock et al. 2011; Wu et al. 2015). These SMBHs most likely grew from smaller seed BHs that formed earlier, but the origin of these seeds remains unclear (Haiman 2006, 2009; Bromm & Yoshida 2011; Greene 2012; Volonteri 2012; Volonteri & Bellovary 2012). Furthermore, feedback and self-regulation of the seeds make the study of their formation and growth even more complex (Milosavljević et al. 2009). The two most promising theories concerning the formation of seed BHs at high redshift are the remnants of massive Population III stars (Madau & Rees 2001; Li et al. 2007; Johnson et al. 2012), and the direct collapse of primordial gas in haloes with virial temperatures $T_{\text{vir}} \gtrsim 10^4 \text{ K}$, the so-called atomic cooling haloes (Bromm

& Loeb 2003; Begelman, Volonteri & Rees 2006; Spaans & Silk 2006).

In the direct collapse scenario, high temperatures are reached in haloes where cooling by molecular hydrogen and metal lines to below $\simeq 10^4 \text{ K}$ has been suppressed, which implies that the only coolant acting on the gas is atomic hydrogen (Omukai 2001; Oh & Haiman 2002). In the case of molecular hydrogen, which naturally forms at the center of the halo, its photo-dissociation can be achieved by an external soft ultraviolet (UV) background in the Lyman-Werner (LW) bands. Previous studies have found that this leads to a nearly isothermal collapse at $T_{\text{vir}} \simeq 10^4 \text{ K}$ due to initially Lyman- α cooling, and subsequently H^- bound-free and free-free emission, when higher densities are reached (Regan & Haehnelt 2009; Latif et al. 2013a; Inayoshi, Omukai & Tasker 2014; Becerra et al. 2015; Chon et al. 2016). High-resolution simulations have shown that, as the gas collapses and reaches densities of $\simeq 10^{17} \text{ cm}^{-3}$, it becomes optically thick to H^- radiation, and a massive protostar with accretion rate $\simeq 1 M_\odot \text{ yr}^{-1}$ forms at the center of the halo (Inayoshi, Omukai & Tasker 2014; Van Borm et al. 2014; Be-

* E-mail: fbecerra@cfa.harvard.edu

cerca et al. 2015; Latif, Schleicher & Hartwig 2016). Due to this high accretion rate, the central object can easily become a supermassive star of $\simeq 10^5 - 10^6 M_\odot$ within a million years (Regan & Haehnelt 2009; Latif et al. 2013a), which later might collapse into a SMBH due to relativistic instabilities (Baumgarte & Shapiro 1999, see also Figure 1).

In this work, we study the physics of the central object when it approaches the optically thick regime. In particular, we investigate the properties of the emerging protostar when the optical depth due to H^- emission becomes unity, thus extending the classical theory of opacity-limited fragmentation developed for present-day star formation (Rees 1976; Low & Lynden-Bell 1976). In addition, we develop an idealized model for the subsequent evolution of the accreting protostar, until the formation of a supermassive object. Based on this modeling of the growing protostar, we deduce parameters for a physically-motivated sink particle algorithm, to be used as a sub-grid recipe in large-scale, hydrodynamic simulations of the formation of SMBH seeds in a fully cosmological context. Such simulations are needed to derive detailed diagnostics for the SMBH assembly process at high redshifts, to be probed with next-generation observational facilities (Pacucci et al. 2015), such as the *James Webb Space Telescope (JWST)*, the *ATHENA* X-ray mission, and the *Laser Interferometer Space Antenna (LISA)* gravitational-wave observatory.

2 PHYSICS OF THE OPACITY LIMIT

2.1 Classical picture

In the theory of star formation, it has been a long-standing quest to understand the limits to fragmentation in a given cloud setting. An influential idea was that fragmentation proceeds hierarchically in a collapsing cloud, as the Jeans mass decreases with increasing density, as long as isothermality roughly holds (Hoyle 1953). The minimum fragment mass is then set by the scale when opacity prevents the release of the gravitational, compressional heat, such that the Jeans mass would increase again upon further compression (Rees 1976; Low & Lynden-Bell 1976). Fragmentation can be seeded in a number of ways, including from non-spherical perturbations of the Larson-Penston solution (Hanawa & Matsumoto 2000; Lai 2000). We here follow a similar reasoning, applied to the peculiar conditions of isothermally collapsing primordial gas in atomic cooling haloes. Our goal is to robustly derive the characteristic density n_F , mass M_F and radius R_F of the emerging protostar, when the gas first becomes optically thick. These values will mark the initial stage in the build-up process of the supermassive object.

We start by considering the simple relation between these three quantities:

$$M_F = \frac{4\pi}{3} \frac{m_H}{X} n_F R_F^3, \quad (1)$$

where we have used $\rho = m_H n / X$, with $X = 0.76$ being the primordial hydrogen mass fraction, to translate total mass density to hydrogen number density.

We furthermore assume that the optically thick cloud is gravitationally bound, such that the characteristic mass

is of order the Jeans mass M_J ,

$$M_F \simeq M_J = \left(\frac{\pi k_B}{G m_H \mu} \right)^{3/2} T^{3/2} n_F^{-1/2}, \quad (2)$$

where $\mu \simeq 1.22$ is the mean molecular weight for a fully-neutral primordial mixture of atomic hydrogen and helium.

Finally, we need to account for energy equilibrium. The energy that is to be radiated away originates in the gravitational collapse of the cloud. In this case, the gravitational energy is emitted in a free-fall time, $t_{\text{ff}} = \sqrt{3\pi/32G\rho}$, as long as the gas remains optically thin to its cooling radiation. From basic thermodynamical considerations, this emission can be modeled as a fraction, $f \lesssim 1$, of the energy radiated from the surface of an equivalent blackbody at the same temperature. Hence, we can equate these two quantities, obtaining:

$$\frac{3}{2} \left(\frac{4\pi}{3} R_F^3 \right) \frac{n_F k_B T}{t_{\text{ff}}} = f 4\pi R_F^2 \sigma_{\text{SB}} T^4, \quad (3)$$

where σ_{SB} is the Stefan-Boltzmann constant.

We then proceed to solve the system of Equations 1, 2, and 3 as a function of the temperature and radiative efficiency f :

$$n_F \simeq 3.57 \times 10^{17} f \left(\frac{T}{8000\text{K}} \right)^{5/2} \text{ cm}^{-3} \quad (4)$$

$$R_F \simeq 0.24 f^{-1} \left(\frac{T}{8000\text{K}} \right)^{-3/4} \text{ au} \quad (5)$$

$$M_F \simeq 0.07 f^{-1/2} \left(\frac{T}{8000\text{K}} \right)^{1/4} M_\odot, \quad (6)$$

where we have normalized T to the typical value of isothermally collapsing gas in an atomic cooling halo. A similar argument for its convergence towards a universal track in the $n - T$ plane on which the gas cloud becomes optically thick to any continuum opacities has been discussed by Omukai et al. (2005).

The expression for the minimum fragment mass reproduces the scalings from the classical theory, but is an order of magnitude larger than for normal stars (e.g. Low & Lynden-Bell 1976; Rees 1976). This contrast reflects the significant difference in temperature in the two respective environments ($T \simeq 10^4$ K vs. 10 K).

2.2 Detailed modeling: One-zone model

The argument above operates with fundamental limits to the cooling ability of gas, set by thermodynamics. Next, we will gain further insight by considering the detailed physics of H^- opacity, based on the actual microphysical cross section for this process. To this extent, we use a one-zone model for the collapse of gas into an atomic cooling halo. Specifically, we implement the chemistry network applied in Inayoshi, Omukai & Tasker (2014) and introduced in Inayoshi, Haiman & Ostriker (2016), which we describe in more detail below. We proceed to find the density at which the cooling and heating rates are equal, which lets us calculate the properties of the gas at the point when it first becomes optically thick to its cooling radiation.

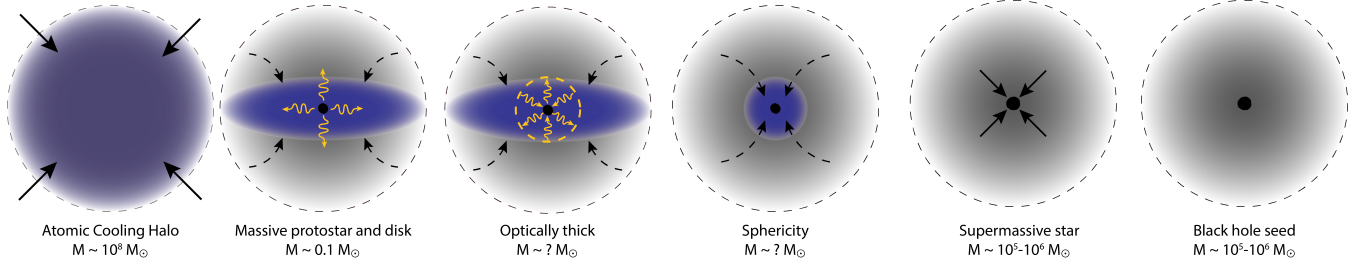


Figure 1. Overview of the formation of a supermassive black hole seed. An atomic cooling halo of virial (total) mass $M \simeq 10^8 M_\odot$ and exposed to strong Lyman-Werner background radiation collapses. The gas reaches the optically thick regime first on small scales, such that a central protostar of initial mass $M \simeq 0.1 M_\odot$ and accretion rate $\dot{M} \simeq 1 M_\odot \text{ yr}^{-1}$ is formed, surrounded by a disk-like structure. Photons coming from the protostar due to accretion are radiated away, until the gas becomes optically thick to H^- radiation at intermediate scales. Eventually, the central object eats up the entire disk and tends toward sphericity, although the mass of the object at each of these later stages still remains to be determined. The massive protostar keeps accreting the surrounding gas and becomes a supermassive star of $M \simeq 10^5 - 10^6 M_\odot$ after $\simeq 10^5 - 10^6 \text{ yr}$. Finally, it collapses into a massive black hole seed due to relativistic instabilities.

2.2.1 Chemistry

The H^- cooling rate is estimated by integrating emissivities and opacities over two frequency ranges: 0-0.75 eV and 0.75-13.6 eV, called “low” and “high” frequency, respectively. The distinction between the two ranges is needed to calculate the cooling rate after the gas becomes opaque to photons in the high frequency regime due to Rayleigh scattering, but is still optically thin to photons in the low frequency regime. Optically thin cooling rates for both high and low frequency regimes are written as $\Lambda_{\text{thin}}^{\text{hf}} = k^{\text{hf}} n_{\text{HI}} n_e$ and $\Lambda_{\text{thin}}^{\text{lf}} = k^{\text{lf}} n_{\text{HI}} n_e$, respectively. The cooling rate coefficients are given by

$$k^{\text{lf}} = 0.2345 \times \frac{T_3^{2.265}}{1 + 0.0360 T_3^{2.149}} \times 10^{-28} \text{ erg cm}^3 \text{ s}^{-1} \quad (7)$$

$$k^{\text{hf}} = 10^{-27} T_3 \times (1.4924 + 0.07815 T_3 + 0.0063 T_3^2) \times (1 - 0.1535 T_3^{0.5}) \text{ erg cm}^3 \text{ s}^{-1} \quad (8)$$

where $T_3 = T/10^3 \text{ K}$.

Next, we need to estimate the Planck mean opacity for the H^- free-free emission in both the low ($\kappa_{\text{ff,P}}^{\text{lf}}$) and high ($\kappa_{\text{ff,P}}^{\text{hf}}$) frequency regime, and for the H^- bound-free emission for the high ($\kappa_{\text{bf,P}}^{\text{hf}}$) frequency regime:

$$\kappa_{\text{ff,P}}^{\text{lf}} = \frac{10^{-28}}{T_3} \times 28.8 \times \frac{T_3^{-0.88}}{1 + 27.86 T_3^{-2.15}} \text{ cm}^{-1} \quad (9)$$

$$\kappa_{\text{ff,P}}^{\text{hf}} = \frac{10^{-29}}{T_3^{2.5}} \exp\left(\frac{-8.761}{T_3}\right) \times 2.868 T_3^{-0.3326} \times (1 + 2.544 T_3^{1.1413} - 2.3369 T_3^{1.162}) \text{ cm}^{-1} \quad (10)$$

$$\kappa_{\text{bf,P}}^{\text{hf}} = \frac{10^{-11}}{T_3^{1.5}} \exp\left(\frac{-8.761}{T_3}\right) \times 5.850 \times (1 - 0.1042 T_3^{0.9419} + 0.0727 T_3^{1.0278}) \text{ cm}^{-1} \quad (11)$$

In addition, we calculate the Rosseland mean opacity for H^- free-free emission in the low frequency regime as:

$$\kappa_{\text{ff,R}}^{\text{lf}} = 10^{-44} T^2 \times 0.4054 T_3^{-8.180} \times \left(\frac{1 + 5.552 T_3^{5.381} + 1.234 T_3^{8.753}}{1 + 0.0296 T_3^{1.180}} \right) \text{ cm}^{-1} \quad (12)$$

Finally, we also estimate the opacity due to Rayleigh

scattering for the high frequency regime as

$$\kappa_{\text{Ray}}^{\text{hf}} = 10^{-42} \exp\left(\frac{8.761}{T_3}\right) \times T_3^{3.5} \times 1.206 \times \left(\frac{T_3^{0.750}}{1 + 0.139 T_3^{1.204}} \right) \text{ cm}^{-1} \quad (13)$$

The total opacities for both regimes can then be written as $\kappa_{\text{R}}^{\text{hf}} = \kappa_{\text{Ray}}^{\text{hf}}$, $\kappa_{\text{R}}^{\text{lf}} = \kappa_{\text{ff,R}}^{\text{lf}}$, $\kappa_{\text{P}}^{\text{hf}} = \kappa_{\text{ff,P}}^{\text{hf}} + \kappa_{\text{bf,P}}^{\text{hf}}$, and $\kappa_{\text{P}}^{\text{lf}} = \kappa_{\text{ff,P}}^{\text{lf}}$. Now we can write the optically thick H^- cooling rate as a function of the optically thin cooling rates and the opacities:

$$\Lambda_{\text{H}^-} = \frac{\Lambda_{\text{thin}}^{\text{hf}}}{1 + 3\kappa_{\text{P}}^{\text{hf}} \kappa_{\text{R}}^{\text{hf}} \lambda_{\text{J}} \lambda_{\text{J}}} + \frac{\Lambda_{\text{thin}}^{\text{lf}}}{1 + 3\kappa_{\text{P}}^{\text{lf}} \kappa_{\text{R}}^{\text{lf}} \lambda_{\text{J}} \lambda_{\text{J}}} \quad (14)$$

Here $\lambda_{\text{J}} \simeq c_s t_{\text{ff}}$ is the Jeans length, with $c_s = \sqrt{\gamma k_B T / \mu m_{\text{H}}}$ being the sound speed.

2.2.2 Critical density

Next, we wish to find the critical density at which the H^- cooling rate and the adiabatic heating rate become identical. The latter can be calculated analytically as

$$\Gamma \simeq \frac{n k_B T}{t_{\text{ff}}}, \quad (15)$$

where we use the density and temperature from the one-zone model outputs as values for n and T . The former can be expressed in terms of the numerical fit given by Equation 14, but due to the complexity of this equation we would like to find a simpler expression. For that, we consider that the cooling rate can be written as

$$\tilde{\Lambda}_{\text{H}^-} = k_{\text{H}^-} E_\gamma n_{\text{HI}} n_e f_{\text{esc}} e^{-\tau_{\text{T}}}, \quad (16)$$

where $E_\gamma = 3.53 \text{ eV}$ is the approximate energy of the emitted photon, $k_{\text{H}^-} = 1.4 \times 10^{-18} T^{0.928} \exp(-T/1.62 \times 10^4) \text{ cm}^3 \text{ s}^{-1}$ is the chemical rate of H^- formation, $\tau_{\text{T}} = \sigma_T n_e \lambda_{\text{J}} / 2$ represents the Thomson opacity, $f_{\text{esc}} = 1/(1 + \tau_{\text{H}^-}^2)$ is the escape fraction, and τ_{H^-} denotes the optical depth due to H^- .

The optical depth to H^- radiation can easily be calculated from Equations 8-13 for both low and high frequency

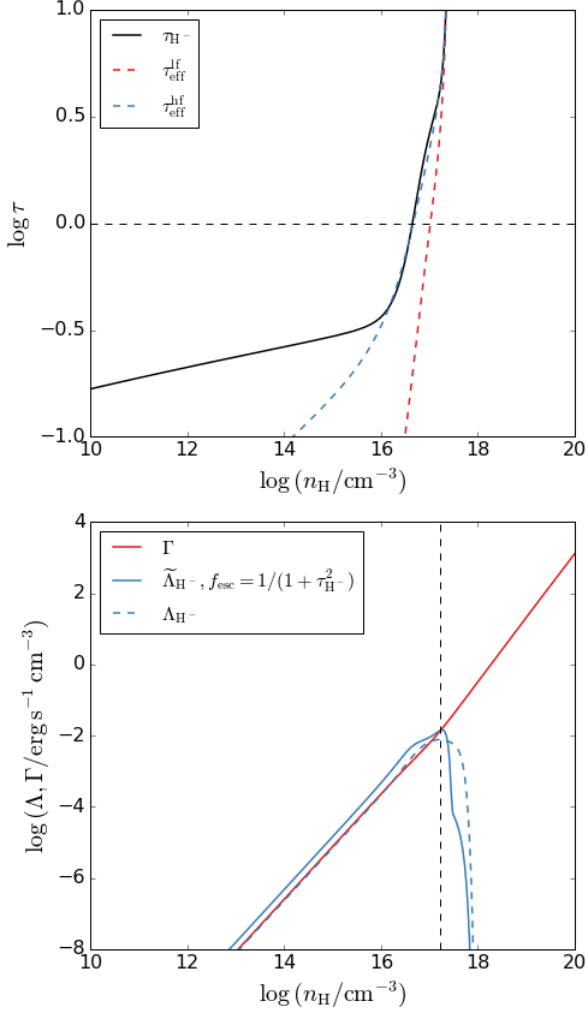


Figure 2. Numerical and analytical fits for our one-zone model. *Top panel:* Gas optical depth as a function of the number density. The numerical fits for the low- and high-frequency effective opacities, $\tau_{\text{eff}}^{\text{lf,hf}}$, are shown in red and blue dashed lines, respectively. Our analytical fit is plotted in solid black line and is given by Equation 17. The point where the gas becomes optically thick ($\tau \simeq 1$) is indicated by a horizontal black dashed line. *Bottom panel:* Heating (red) and cooling (blue) rates as a function of number density, where solid lines represent the approximate expressions given by Equations 15 and 16, while the dashed line indicates the full expression for the cooling rate as expressed by Equation 14. The vertical black dashed line shows the point at which the analytical cooling and heating rates intersect.

ranges. These quantities are shown in the top panel of Figure 2 in blue and red dashed lines, respectively. The effective optical depth for each frequency range is defined as $\tau_{\text{eff}}^{\text{lf,hf}} = \sqrt{3\kappa_{\text{P}}^{\text{lf,hf}}\kappa_{\text{R}}^{\text{lf,hf}}\lambda_{\text{J}}\lambda_{\text{J}}}$ (Inayoshi, Haiman & Ostriker 2016), where $\kappa_{\text{P}}^{\text{lf,hf}}$ and $\kappa_{\text{R}}^{\text{lf,hf}}$ were defined at the end of Section 2.2.1. From this plot we can see that the opacity for high frequencies surpasses unity at lower densities, and we choose this value to calculate the H^- cooling rate. To simplify our calculations, we fit an analytical model to the high

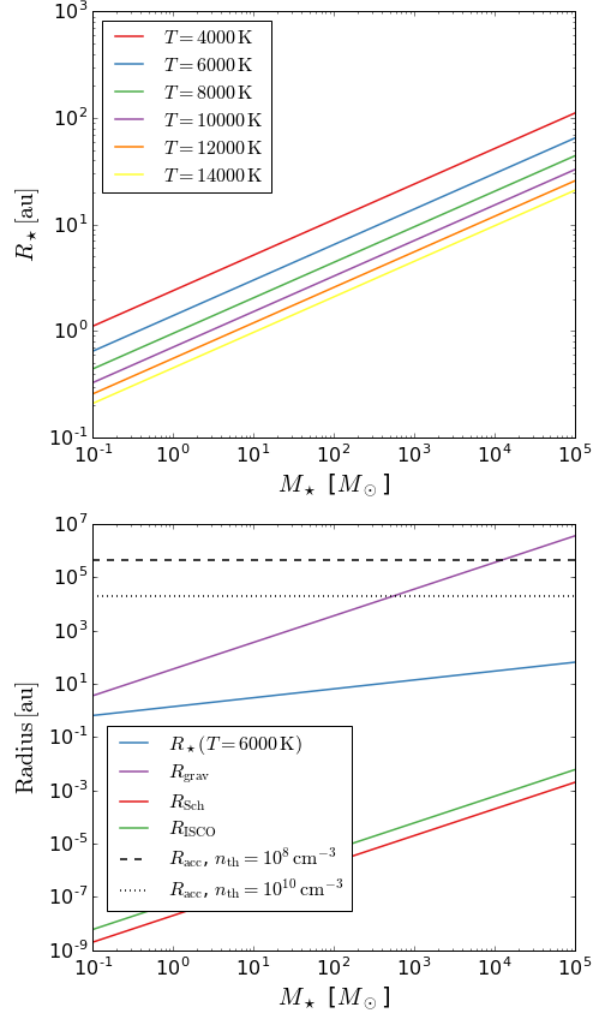


Figure 3. *Top panel:* Stellar radius as a function of stellar mass and surface temperature, given by Equation 19 and assuming a typical mass accretion rate of $\dot{M}_{\star} \simeq 1M_{\odot} \text{ yr}^{-1}$. Colors show the radius for $T = 4000$ K (red), 6000 K (blue), 8000 K (green), 10000 K (purple), 12000 K (orange), and 14000 K (yellow), respectively. *Bottom panel:* Significant length scales for the problem as a function of the stellar mass: stellar radius for a typical temperature of $T \simeq 6000$ K (blue), Schwarzschild radius (red), radius of the innermost stable circular orbit (ISCO, green), and gravitational radius (purple). In addition we have included the accretion radius as defined in Equation 22 for a density threshold of $n_{\text{th}} = 10^8 \text{ cm}^{-3}$ (black dashed) and $n_{\text{th}} = 10^{10} \text{ cm}^{-3}$ (black dotted).

frequency opacity given by

$$\tau_{\text{H}^-} = \frac{2 \times 10^{-14} \text{ cm}^2}{(T/10^{3.6} \text{ K})^3} n_{\text{H}} - \lambda_{\text{J}}/2, \quad (17)$$

and shown in black line in the top panel of Figure 2.

We then replace τ_{H^-} (Equation 17) in the expression for $\tilde{\Lambda}_{\text{H}^-}$ (Equation 16) and obtain an analytical form for the cooling rate, which is plotted in the bottom panel of Figure 2 as a blue solid line. Additionally, we have also plotted the heating rate (Equation 15) in solid red and the output from our one-zone model for the cooling rate in dashed blue lines. By equating both rates, we obtain the density

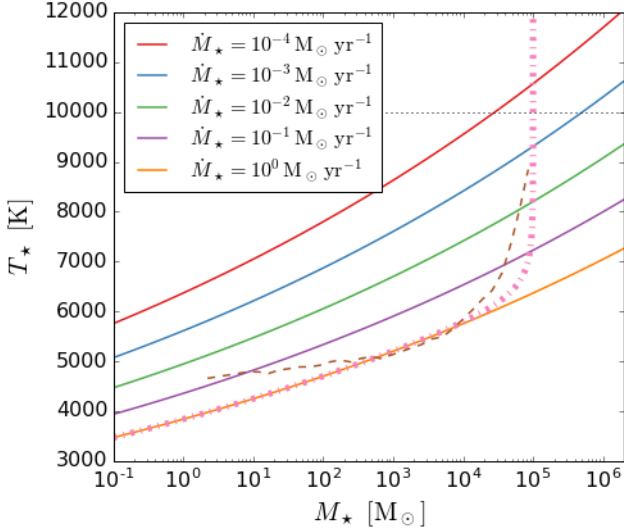


Figure 4. Photospheric temperature as a function of stellar mass and accretion rate. Colors show the temperature evolution for $\dot{M}_* = 10^{-4}$ (red solid), 10^{-3} (blue solid), 10^{-2} (green solid), 10^{-1} (purple solid), and $1 \text{ M}_\odot \text{ yr}^{-1}$ (orange solid) based on Equation (23b) from Stahler, Palla & Salpeter (1986). Additionally, we plot a time-dependent accretion rate of the form $\dot{M}_*(t) = 1 \text{ M}_\odot \text{ yr}^{-1} e^{-t/t_{\text{ff},0}}$ (pink dash-dotted), as an illustrative case, and the results from Hosokawa et al. (2013) (brown dashed). Note that, although both curves seem to agree well, the physical reasons for the rise in temperature are different (see text for more details). Black dotted line represent the ionizing temperature, $T_{\text{ion}} \simeq 10000 \text{ K}$, at which the photosphere starts to emit non-negligible amounts of H ionizing radiation. The surface temperature of the protostar does not become high enough to start emitting hard UV radiation until quite late in the mass build-up. Hence, we can safely neglect its effect on the evolution of the central object early on.

$n_{\text{crit}} \simeq 1.7 \times 10^{17} \text{ cm}^{-3}$ at which the gas becomes optically thick to H^- cooling. Note that this density, here derived from consideration of the detailed microphysics involved, is very similar to the estimate in Section 2.1. We can thus robustly characterize the conditions at the onset of super-massive protostar formation.

2.3 Subsequent evolution

Once the central object starts growing, we need to consider the gas being accreted from the surroundings to describe its evolution. In that case, the energy powering the object will dominantly come from accretion rather than self-gravitating collapse. To account for that, we modify the left hand side of Equation 3 and consider only accretion luminosity:

$$\frac{GM_* \dot{M}_*}{R_*} = f 4\pi R_*^2 \sigma_{\text{SB}} T_*^4. \quad (18)$$

Thus neglecting any internal sources of stellar energy is justified during the early stages of protostellar evolution, where accretion rates are huge, such that the accretion timescale, $t_{\text{acc}} = M_*/\dot{M}_*$, is shorter than the Kelvin-Helmholtz timescale, $t_{\text{KH}} = GM_*^2/R_* L_*$, $t_{\text{acc}} \lesssim t_{\text{KH}}$. At some point toward the later evolution of the system, when

the accretion rate begins to drop significantly, this idealizing assumption will break down, and the protostellar model needs to be augmented by internal contributions (e.g., see Stacy, Bromm & Lee 2016). The precise protostellar mass where KH contraction begins to dominate sensitively depends on the detailed geometry of the accretion flow (Hosokawa, Yorke & Omukai 2010; Hosokawa, Omukai & Yorke 2012; Hosokawa et al. 2013). Determining this geometry is a major goal of future high-resolution simulations with cosmological boundary conditions.

We can then solve for R_* as a function of the mass of the star, M_* , accretion rate, \dot{M}_* , and surface temperature, T_* :

$$R_* \simeq 1.4 f^{-1/3} \left(\frac{M_*}{\text{M}_\odot} \right)^{1/3} \left(\frac{\dot{M}_*}{\text{M}_\odot \text{ yr}^{-1}} \right)^{1/3} \left(\frac{T_*}{6000 \text{ K}} \right)^{-4/3} \text{ au}. \quad (19)$$

We plot this expression for temperatures $T_* = 4000 \text{ K}$ (red), 6000 K (blue), 8000 K (green), 10000 K (purple), 12000 K (orange), and 14000 K (yellow) as a function of stellar mass in the top panel of Figure 3, where we have assumed $\dot{M}_* \simeq 1 \text{ M}_\odot \text{ yr}^{-1}$. Note that we have normalized the photospheric temperature in this expression to a characteristic value, $T_* \simeq 6000 \text{ K}$, imposed by the strong temperature dependence of the H^- opacity (Stahler, Palla & Salpeter 1986; Omukai & Palla 2003).

In the bottom panel, we compare the stellar radius (blue solid) for $T_* \simeq 6000 \text{ K}$ to other important length scales in our problem. Among them, we consider the Schwarzschild radius, $R_{\text{Sch}} = 2GM_*/c^2$ (red solid), the innermost stable circular orbit (ISCO) radius, $R_{\text{ISCO}} = 6GM_*/c^2$ (green solid), and the gravitational radius, $R_{\text{grav}} = 2GM_*/c_s^2$ (purple solid). The protostar's radius grows from $R_* \simeq 0.65 \text{ au}$ at $M_* \simeq 0.1 \text{ M}_\odot$ to $R_* \simeq 65 \text{ au}$ at $M_* \simeq 10^5 \text{ M}_\odot$, well below the gravitational radius, but above both the Schwarzschild and ISCO radii for the whole range of masses.

One factor that might dramatically influence the evolution described in this section is the radiation coming from the central protostar. Here, we have assumed a constant temperature for simplicity, in effect the characteristic value due to the physics of H^- opacity. Throughout the evolution of the central object, however, its temperature will vary and eventually reach a point where radiative feedback becomes important. Previous studies have analyzed the formation of primordial supermassive stars in the rapid mass accretion regime and have found that the effective temperature of the object remains well below 10^4 K , for protostellar masses up to 10^4 M_\odot , or so (Hosokawa, Omukai & Yorke 2012; Hosokawa et al. 2013), suggesting that radiative feedback might not become important up to those mass scales.

It is useful to explore the likely temperature evolution of the growing supermassive protostar, in response to a realistic mass accretion history provided by a cosmological simulation. To this extent, we consider the photospheric temperature, given by the general 1D radiation hydrodynamics calculation of Stahler, Palla & Salpeter (1986):

$$T_* \simeq 3836 \text{ K} \left(\frac{M_*}{\text{M}_\odot} \right)^{0.044} \left(\frac{\dot{M}_*}{\text{M}_\odot \text{ yr}^{-1}} \right)^{-0.055}. \quad (20)$$

We have plotted this relation in Figure 4 for accretion rates of 10^{-4} (red solid), 10^{-3} (blue solid), 10^{-2} (green solid), 10^{-1} (purple solid), and $1 \text{ M}_\odot \text{ yr}^{-1}$ (orange solid). As it can

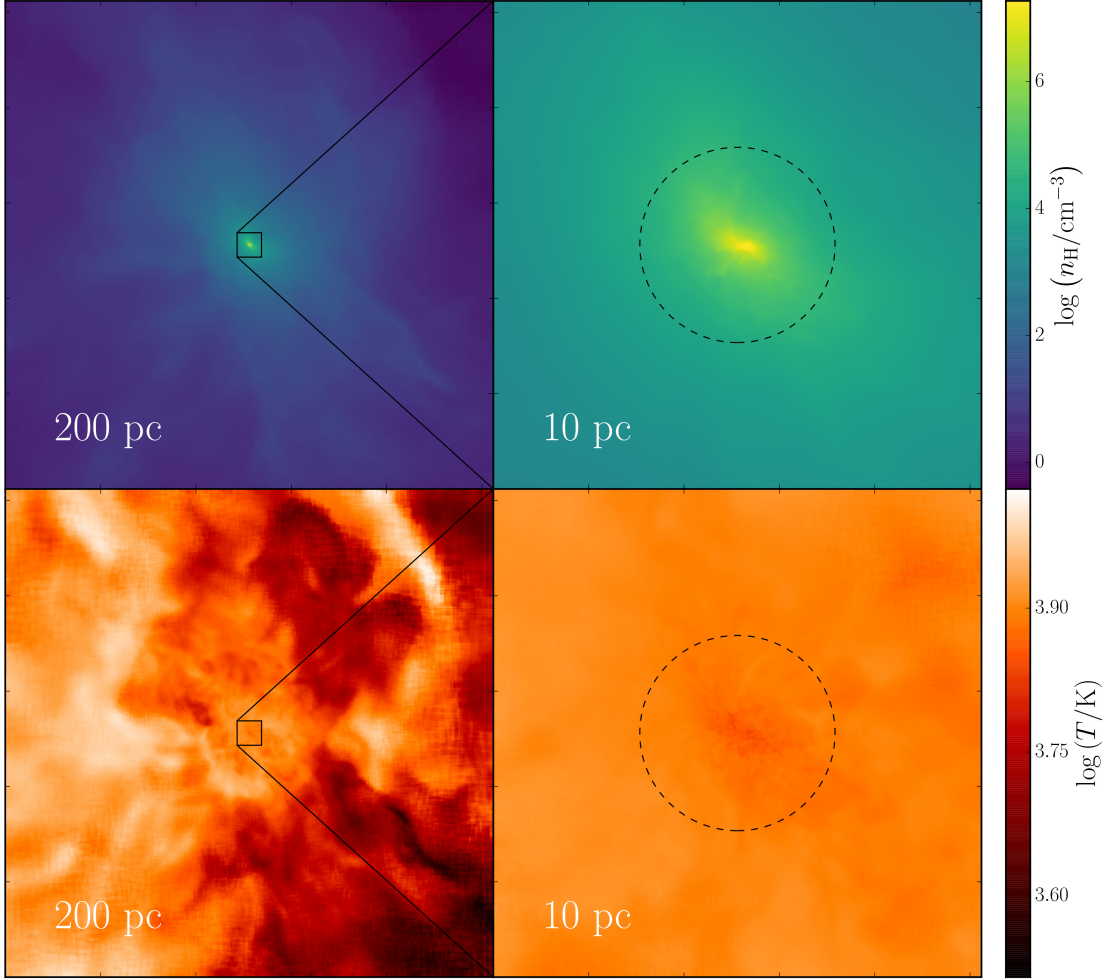


Figure 5. Density (*top*) and temperature (*bottom*) projections of the central 200 (left) and 10 pc (right) for a low-resolution simulation of an atomic-cooling halo when the highest density cell first reaches 10^8 cm^{-3} . From Equation 22, the accretion radius at this point is $R_{\text{acc}} \simeq 2 \text{ pc}$, which is plotted in dashed black lines in both panels of the right column. At scales of 200 pc the cloud has an irregular morphology but it becomes nearly spherical on the smallest scales. The presence of turbulence can be deduced from the filamentary structure in the large-scale temperature map.

be seen, the temperature at which the photosphere begins to emit H-ionizing radiation, $T_{\text{ion}} \simeq 10000 \text{ K}$ (black dotted), is only reached at masses $10^4 M_{\odot} \lesssim M_{\star} \lesssim 10^6 M_{\odot}$ for low accretion rates of $\dot{M}_{\star} \simeq 10^{-3} - 10^{-4} M_{\odot} \text{ yr}^{-1}$.

In addition to our constant accretion rate assumption, we have included a time-dependent toy model of the form $\dot{M}_{\star}(t) = 1 M_{\odot} \text{ yr}^{-1} e^{-t/t_{\text{ff},0}}$ (pink dash-dotted line), with $t_{\text{ff},0} = 10^5 \text{ yr}$ being the free-fall time in the core of the atomic cooling halo and $M_{\star}(t=0) = M_{\text{F}} \simeq 0.1 M_{\odot}$. We also compare with the Hosokawa et al. (2013) results for the effective temperature T_{eff} at $\dot{M}_{\star} \simeq 1 M_{\odot} \text{ yr}^{-1}$ (brown dashed line). Both models agree well, but in the former case the increasing effective temperature is due to a drop in the accretion rate, while in the latter case this is a result of the decrease in the opacity because of the expansion of the stellar radius. Similar to the case of constant \dot{M}_{\star} , none of these models reach T_{ion} during the evolution of the protostar up to masses of $10^5 M_{\odot}$. Since the photospheric temperature at the characteristic accretion rate $\dot{M}_{\star} \simeq 1 M_{\odot} \text{ yr}^{-1}$ never surpasses 10^4 K , we can safely neglect photo-ionization feed-

back from the central protostar during most of its evolution. This radiation only becomes important for accretion rates a few orders of magnitude lower than $1 M_{\odot} \text{ yr}^{-1}$, or for masses $M_{\star} \simeq 10^5 M_{\odot}$ in the case of our time-dependent model.

Finally, combining Equations 19 and 20 we can calculate the radius of the star as a function of the mass and accretion rate:

$$R_{\star} \simeq 2.5 f^{-1/3} \left(\frac{M_{\star}}{M_{\odot}} \right)^{0.27} \left(\frac{\dot{M}_{\star}}{M_{\odot} \text{ yr}^{-1}} \right)^{0.41} \text{ au}, \quad (21)$$

where we have recovered the same exponents described in Stahler, Palla & Salpeter (1986).

3 LESSONS FOR SINK ALGORITHM

3.1 Accretion radius

In the case of numerical simulations, the evolution of the central protostar requires either the implementation of sink particles (e.g. Latif et al. 2013b) or an artificially stiffened

equation of state (e.g. Hirano & Bromm 2016). For the former, we can use the treatment in the previous section of the protostellar evolution to construct a physically motivated sub-grid model. In this case, we consider that the gas crossing the accretion radius of the sink particle reaches the stellar surface in about a free-fall time, which implies that density and radius are related by the expression $n \propto r^{-3/2}$. If we apply this to the optically thick regime, then we impose a normalization condition at $r = R_F$, and derive an expression for the accretion radius given by

$$R_{\text{acc}} = R_F \left(\frac{n_F}{n_{\text{th}}} \right)^{2/3}, \quad (22)$$

where n_{th} is the threshold density at which we want to insert the sink particle.

We calculate the accretion radius for two values of the threshold density: $n_{\text{th}} = 10^8 \text{ cm}^{-3}$ and $n_{\text{th}} = 10^{10} \text{ cm}^{-3}$, which gives $R_{\text{acc}} \simeq 4.2 \times 10^5 \text{ au}$ and $R_{\text{acc}} \simeq 2 \times 10^4 \text{ au}$, respectively. The two quantities are shown in the bottom panel of Figure 3 as black dashed line for the former and black dotted line for the latter. In both cases the accretion radius is larger than the stellar radius (calculated at $T = 6000 \text{ K}$) in the mass range $0.1 - 10^5 M_\odot$. This ensures that the central star, modeled as a sink particle, will always be enclosed by the accretion radius during its evolution, from its formation until it becomes a supermassive star.

3.2 Cosmological boundary conditions

We perform a low-resolution simulation of the collapse of an atomic cooling halo following a similar approach to the one described in Becerra et al. (2015). We start from cosmological initial conditions and follow the evolution of the halo until the highest density cell reaches the threshold density $n_{\text{th}} = 10^8 \text{ cm}^{-3}$. We show the number density (top) and temperature (bottom) projections of the central object at scales of 200 (left) and 10 pc (right) at that instant in time in Figure 5. At large scales the cloud shows an irregular morphology, but it becomes nearly spherical at scales of $\simeq 10 \text{ pc}$. This implies that the object reaches spherical symmetry at scales larger than the accretion radius at that instant ($R_{\text{acc}} \simeq 2 \text{ pc}$, as calculated in Section 3.1), which is plotted in black dashed lines.

Finally, we analyze the accretion rate onto the object at the moment when the simulation reaches the threshold density in Figure 6. The radial profile of the accretion rate is shown as red solid line, which is calculated as $\dot{M} = -4\pi r^2 \rho v_{\text{rad}}$, with r the distance to the highest density cell, ρ the mass density of hydrogen, and v_{rad} the radial component of the velocity. For reference, we have also included the Shu accretion rate for spherical collapse, $\dot{M}_{\text{Shu}} \simeq 0.975 c_s^3 / G$ (Shu 1977), and the Larson-Penston accretion rate for dynamical collapse, $\dot{M}_{\text{LP}} \simeq 46.9 c_s^3 / G$ (Larson 1969; Penston 1969), as blue and green dotted lines, respectively. The mass accretion reaches a maximum of $\dot{M} \simeq 1.4 M_\odot \text{ yr}^{-1}$ at $r \simeq 0.5 \text{ pc}$ and then it decreases to values $\dot{M} \simeq 0.1 M_\odot \text{ yr}^{-1}$ at larger scales. Up to scales of $\simeq 15 \text{ pc}$, its value lies in between the Shu and the Larson-Penston accretion rates, which remain roughly constant at $\dot{M}_{\text{Shu}} \simeq 0.18 M_\odot \text{ yr}^{-1}$ and $\dot{M}_{\text{LP}} \simeq 8.5 M_\odot \text{ yr}^{-1}$ for the whole radial range. At the accretion radius (shown as a vertical black dashed line), the value of the mass infall

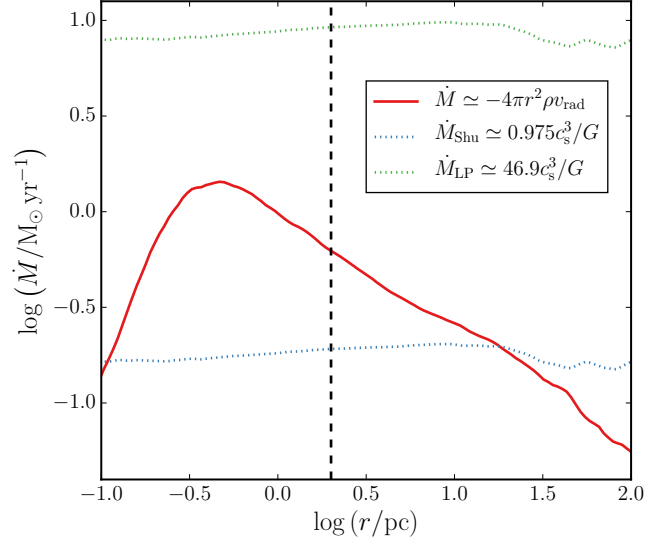


Figure 6. Mass accretion rate as function of radius, centered on the highest density cell of the halo. The mass accretion rate reaches a maximum of $\dot{M} \simeq 1.4 M_\odot \text{ yr}^{-1}$ at $r \simeq 0.5 \text{ pc}$, and then it decreases to $\dot{M} \simeq 0.1 M_\odot \text{ yr}^{-1}$ at a radial distance of $r \simeq 100 \text{ pc}$. Note that the spatial non-constancy of \dot{M} implies non-steady state conditions during the initial infall. At the accretion radius (vertical dashed line) the value of the mass infall rate is $\dot{M} \simeq 0.6 M_\odot \text{ yr}^{-1}$. For comparison, we have also plotted $\dot{M}_{\text{Shu}} \simeq 0.975 c_s^3 / G$ (blue dotted line), which stays between $0.1 M_\odot \text{ yr}^{-1}$ and $0.2 M_\odot \text{ yr}^{-1}$, and $\dot{M}_{\text{LP}} \simeq 46.9 c_s^3 / G$ (green dotted line), which oscillates around $8.5 M_\odot \text{ yr}^{-1}$.

rate is $\dot{M} \simeq 0.6 M_\odot \text{ yr}^{-1}$, which is consistent with the values assumed throughout this study.

4 SUMMARY AND CONCLUSIONS

In this paper we have developed a model for the early evolution of SMBH seeds. After the formation of the initial protostar the surrounding gas becomes optically thick to H^- radiation, at which point we can robustly calculate the properties of the object using the equations of hydrostatic and thermal equilibrium. From that we obtain a characteristic density, radius, and mass of $n_F \simeq 4 \times 10^{17} \text{ cm}^{-3}$, $R_F \simeq 0.25 \text{ au}$, and $M_F \simeq 0.1 M_\odot$, respectively, for a temperature $T = 8000 \text{ K}$. An alternative approach to model the same situation is to use one-zone models. In that case we adopt the numerical fits for the H^- cooling rate and opacity described in Inayoshi, Haiman & Ostriker (2016). Combined with the adiabatic heating rate, we can then calculate the critical density at which the gas becomes optically thick as the density where the cooling and heating rates are identical. This results in $n_{\text{crit}} \simeq 1.7 \times 10^{17} \text{ cm}^{-3}$, consistent with the previous estimate. Hence we can robustly characterize the properties of the protostar in the initial optically thick regime.

The early stages of protostellar evolution, where $t_{\text{acc}} \lesssim t_{\text{KH}}$, are described by the accretion of material onto the central object. For this case, we derive an expression for the protostellar radius as a function of the mass and accretion

rate. Using a characteristic value of $\dot{M}_* \simeq 1\text{M}_\odot \text{yr}^{-1}$ for the accretion rate, we find that the protostellar radius grows as $R_* \propto \dot{M}_*^{1/4}$. For the case of a SMBH seed, the radius varies from $R_* \simeq 0.65\text{au}$ at $\dot{M}_* \simeq 0.1\text{M}_\odot$ to $R_* \simeq 65\text{au}$ at $\dot{M}_* \simeq 10^5\text{M}_\odot$. For the surface temperature of the object, we base our analysis on the prescription of Stahler, Palla & Salpeter (1986), deducing that it remains well below the ionizing temperature of $T_{\text{ion}} \simeq 10^4\text{K}$ during most of its evolution. We can thus safely neglect UV ionizing radiation until the late stages of the assembly process.

In numerical simulations, SMBH seeds are commonly represented by sink particles. Our model allows us to derive the properties of such particles and implement a physically-motivated sub-grid model for their evolution in hydrodynamical codes. In particular, we derive an expression for the accretion radius (R_{acc}) as a function of the density at which the sink particle is inserted (n_{th}), relating it to the physical conditions on the surface of the protostar. We can thus verify throughout the simulation that the accretion radius is well adjusted, in the sense that it is larger than the stellar radius at every moment during its evolution. This idealized model is valid as long as $t_{\text{acc}} \lesssim t_{\text{KH}}$. We will track these timescales during the actual simulation to determine when the accretion rate becomes low enough that our assumptions break down. At this point, the radiation hydrodynamic effects from an ionizing central source would have to be taken into account.

The ultimate goal of this line of work is to simulate the assembly process of the first supermassive objects in the Universe in an ab-initio fashion. One key question then is: When will this build-up enter a radiation-hydrodynamical phase, where the strong radiative feedback from the growing protostar will eventually turn the object into hyper-luminous beacons from the end of the cosmic dark ages? Those will be probed with next-generation observational facilities, such as the *James Webb Space Telescope (JWST)*, to be launched in 2018. An ideally complementary window into the formation of the first supermassive objects is provided by the gravitational wave signal accompanying the possible merger of binary black holes, which is a prime target for the planned Laser Interferometer Space Antenna (LISA). In light of this suite of next-generation facilities, simulations will have a key role to play in providing physically robust predictions, based on well-motivated sub-grid prescriptions.

ACKNOWLEDGEMENTS

We thank Kazuyuki Omukai for kindly providing permission to use the numerical models for H^- cooling described in Section 2.2.1. KI acknowledges support by the Simons Foundation through the Simons Society of Fellows. VB was supported by NSF grant AST-1413501.

REFERENCES

Baumgarte T. W., Shapiro S. L., 1999, *ApJ*, 526, 941
 Becerra F., Greif T. H., Springel V., Hernquist L. E., 2015, *MNRAS*, 446, 2380
 Begelman M. C., Volonteri M., Rees M. J., 2006, *MNRAS*, 370, 289

Bromm V., Loeb A., 2003, *ApJ*, 596, 34
 Bromm V., Yoshida N., 2011, *ARA&A*, 49, 373
 Chon S., Hirano S., Hosokawa T., Yoshida N., 2016, *ApJ*, 832, 134
 Fan X. et al., 2006, *AJ*, 132, 117
 Fan X. et al., 2003, *AJ*, 125, 1649
 Greene J. E., 2012, *Nature Communications*, 3
 Haiman Z., 2006, *New Astron. Rev.*, 50, 672
 Haiman Z., 2009, *Observing the First Stars and Black Holes*, Thronson H. A., Stiavelli M., Tielens A., eds., p. 385
 Hanawa T., Matsumoto T., 2000, *PASJ*, 52, 241
 Hirano S., Bromm V., 2016, *ArXiv e-prints*
 Hosokawa T., Omukai K., Yorke H. W., 2012, *ApJ*, 756, 93
 Hosokawa T., Yorke H. W., Inayoshi K., Omukai K., Yoshida N., 2013, *ApJ*, 778, 178
 Hosokawa T., Yorke H. W., Omukai K., 2010, *ApJ*, 721, 478
 Hoyle F., 1953, *ApJ*, 118, 513
 Inayoshi K., Haiman Z., Ostriker J. P., 2016, *MNRAS*, 459, 3738
 Inayoshi K., Omukai K., Tasker E., 2014, *MNRAS*, 445, L109
 Johnson J. L., Whalen D. J., Fryer C. L., Li H., 2012, *ApJ*, 750, 66
 Lai D., 2000, *ApJ*, 540, 946
 Larson R. B., 1969, *MNRAS*, 145, 271
 Latif M. A., Schleicher D. R. G., Hartwig T., 2016, *MNRAS*, 458, 233
 Latif M. A., Schleicher D. R. G., Schmidt W., Niemeyer J., 2013a, *MNRAS*, 430, 588
 Latif M. A., Schleicher D. R. G., Schmidt W., Niemeyer J. C., 2013b, *MNRAS*, 436, 2989
 Li Y. et al., 2007, *ApJ*, 665, 187
 Low C., Lynden-Bell D., 1976, *MNRAS*, 176, 367
 Madau P., Rees M. J., 2001, *ApJL*, 551, L27
 Milosavljević M., Bromm V., Couch S. M., Oh S. P., 2009, *ApJ*, 698, 766
 Mortlock D. J. et al., 2011, *Nature*, 474, 616
 Oh S. P., Haiman Z., 2002, *ApJ*, 569, 558
 Omukai K., 2001, *ApJ*, 546, 635
 Omukai K., Palla F., 2003, *ApJ*, 589, 677
 Omukai K., Tsuribe T., Schneider R., Ferrara A., 2005, *ApJ*, 626, 627
 Pacucci F., Ferrara A., Volonteri M., Dubus G., 2015, *MNRAS*, 454, 3771
 Penston M. V., 1969, *MNRAS*, 144, 425
 Rees M. J., 1976, *MNRAS*, 176, 483
 Regan J. A., Haehnelt M. G., 2009, *MNRAS*, 396, 343
 Shu F. H., 1977, *ApJ*, 214, 488
 Spaans M., Silk J., 2006, *ApJ*, 652, 902
 Stacy A., Bromm V., Lee A. T., 2016, *MNRAS*, 462, 1307
 Stahler S. W., Palla F., Salpeter E. E., 1986, *ApJ*, 302, 590
 Van Borm C., Bovino S., Latif M. A., Schleicher D. R. G., Spaans M., Grassi T., 2014, *A&A*, 572, A22
 Volonteri M., 2012, *Science*, 337, 544
 Volonteri M., Bellovary J., 2012, *Reports on Progress in Physics*, 75, 124901
 Wu X.-B. et al., 2015, *Nature*, 518, 512